Marine Life Science & Technology (2023) 5:435–454
https://doi.org/10.1007/s42995-023-00200-2

RESEARCH PAPER

Establishment of a developmental atlas and transgenetic tools in the ascidian *Styela clava*

Boyan Lin[1] · Wenjie Shi[1] · Qiongxuan Lu[1] · Takumi T. Shito[3] · Haiyan Yu[1] · Bo Dong[1,2,4]

Received: 23 January 2023 / Accepted: 28 September 2023 / Published online: 22 November 2023

Abstract

The ascidian *Styela clava* is an ecologically important species that is distributed along coastal regions worldwide. It has a long history as a model animal for evolutionary and developmental biology research owing to its phylogenetic position between vertebrates and invertebrates, and its classical mosaic expression patterns. However, the standard developmental atlas and protocols and tools for molecular manipulation of this organism are inadequate. In this study, we established a standard developmental table and provided a web-based digital image resource for *S. clava* embryogenesis at each developmental stage from fertilized eggs to hatching larvae by utilizing confocal laser microscopy and 3D reconstruction images. It takes around 10 h for fertilized eggs to develop into swimming larvae and 20–30 min to complete the tail regression processes at the metamorphic stage. We observed that the notochord cells in *S. clava* embryos did not produce an extracellular lumen like *Ciona robusta*, but showed polarized elongation behaviors, providing us an ideal comparative model to study tissue morphogenesis. In addition, we established a chemical-washing procedure to remove the chorion easily from the fertilized eggs. Based on the dechorionation technique, we further realized transgenic manipulation by electroporation and successfully applied tissue-specific fluorescent labeling in *S. clava* embryos. Our work provides a standard imaging atlas and powerful genetic tools for investigating embryogenesis and evolution using *S. clava* as a model organism.

Keywords Ascidian · Dechorionation · Developmental atlas · *Styela clava* · Transgenic manipulation

Introduction

Ascidians such as *Halocynthia roretzi*, *Ciona intestinalis*, and *Phallusia mammillata* have long been used as model organisms for studying embryonic development and its underlying regulatory mechanisms (McDougall et al. 2011; Satoh 1994, 2013). Due to the transparent nature of the embryo and its relatively small cell number, Conklin (1905a) used the fertilized oocytes of *S. clava* to track the regularity of cell division based on observations of the specific distribution and allocation of cytoplasmic pigmentum during embryogenesis, and established a cell lineage for embryonic development. Later studies found special mosaic developmental patterns in solitary ascidians such as *Halocynthia roretzi* and *Ciona robusta* (*Ciona intestinalis* type A) (Nishida 2005). In addition, the manipulation of embryos such as the construction of ascidian libraries and transgenes (Corbo et al. 1997), genome assembly at the chromosomal level and transcriptome profiling during development (Dehal et al. 2002; Satou et al. 2019; Wei et al. 2020), gene editing (Christiaen et al. 2009; Sasaki et al. 2014; Small et al. 2007; Stolfi et al. 2014) and other technology platforms, improved the capacity for embryo manipulation at the genetic level. Considering the special evolutionary status (Delsuc et al. 2006) and the comprehensive database (Brozovic et al. 2016; Tassy et al. 2010) of ascadians, research using these

Special Topic: EvoDevo.

Edited by Jiamei.

Boyan Lin and Wenjie Shi have contributed equally to this article.

✉ Bo Dong
bodong@ouc.edu.cn

[1] Fang Zongxi Center, College of Marine Life Sciences, Ocean University of China, Qingdao 266003, China

[2] Laoshan Laboratory, Qingdao 266237, China

[3] Department of Bioscience and Informatics, Faculty of Science and Technology, Keio University, Yokohama 223-8522, Japan

[4] MoE Key Laboratory of Evolution and Marine Biodiversity, Ocean University of China, Qingdao 266003, China

organisms can provide insights into the origin of chordate organs, and how vertebrates evolved from the common ancestor of chordates.

Styela clava is classified as a member of the class Ascidiacea, order Stolidobranchia, and family Styelidae. It was originally described by Herdman (1881) from dredged specimens in the Sea of Okhotsk (Abbott and Johnson 1972). *Styela clava* is a tunicate that shows global environmental adaptation (Dupont et al. 2009; Goldstien et al. 2010; Locke et al. 2007) because of its invasiveness, which may negatively affect native species and cause serious damage to commercial aquaculture such as scallop farming (Davis and Davis 2010). Adults can be collected all year round because of the high tolerance of *S. clava* to a wide range of temperatures (Cinar 2016).

Styela clava adults have multiple gonads, compared to a single gonad in *C. robusta* species. There is no outer covering of follicle cells on the eggs of *S. clava* whereas such a covering is present on the eggs of *Ciona* spp. (Bhattachan et al. 2020). The eggs of *S. clava* are up to 200 microns in diameter with a tough chorion. The fertilized egg needs around 10 h to develop into a hatched larva which acquires complete swimming ability instantly. After a swimming period of about 2.5 h post hatching (hph), adhesion will occur. In contrast, adhesion occurs after about 4.5 h ' swimming period in *C. robusta* (Matsunobu and Sasakura 2015). At around 3 hph, *S. clava* larvae have completed the swimming larval stage and the rapid tail regression process is initiated. Although there are significant structural differences between *S. clava* embryos and other ascidians (Dardaillon et al. 2020; Guignard et al. 2020; Hotta et al. 2007, 2020), detailed images of developmental stages are still needed to better identify the differences between species.

In this study, we constructed a standard three-dimensional (3D) developmental table and collected confocal laser scanning microscopy (CLSM) images of embryogenes in *S. clava* by annotating the morphology at each defined stage sequentially at 23 °C. We also provided a continuous time-lapse movie with standard developmental stages and time duration. Morphometrical information about the length of the tail-to-trunk ratio is also described for each stage. We deposited the raw data on the Resources of Ascidian Morphology Network-based (RAMNe) at https://chordate.bpni.bio.keio.ac.jp/RAMNe/latest/index_styela.html, thereby providing a comprehensive record of the spatiotemporal morphological changes that occur during the early developmental processes of *S. clava*. This enables easy access to 3D angles of each embryo and slices of different layers, and facilitates systematic comparisons of the morphology and development process of *C. robusta* and *A. aspersa* at the same stage, which is valuable for studying chordate development. In addition, we developed an easy procedure to remove the chorion from fertilized eggs by the chemical-washing method and applied tissue-specific fluorescent labeling in *S. clava* embryos.

Results

Developmental stages of *S. clava*

We observed and defined 22 stages of embryogenesis and larval development in *S. clava,* from egg fertilization to hatching of larvae, based on morphology and developmental events. For each stage, we provide corresponding differential interference contrast (DIC) images of embryos with a chorion (Supplementary Fig. S1), DIC images of embryos without a chorion (Supplementary Fig. S2), and 3D reconstruction images of embryos without a chorion using Phalloidin 488 staining (Fig. 1). Embryogenesis was partitioned into six periods: zygote, cleavage, gastrula, neurula, tailbud, and larva.

The criteria for staging of the zygote to cleavage period (stages 1–10) depend on the embryo shape and the quantity of cells. After stage 10, the criteria are based primarily on embryo morphology, the tail-to-trunk ratio (recorded after stage 15), and distinct developmental event features referencing those previously described for *C. robusta* (Hotta et al. 2007).

The "standard development time" (in hours) was established to represent the normalized hours post-fertilization (hpf) at 23 °C by converted staging information. The optimal incubation temperatures were between 16 and 23 °C, based on our observations and previously published research (Cinar 2016). The hatching times, which were determined by time-lapse imaging of chorionic embryos co-cultured with dechorionic embryos at different temperatures, were 10 ± 0.50 h at 23 °C, 12 ± 0.38 h at 20 °C, 17 ± 0.48 h at 18 °C, and 20 ± 0.43 h at 16 °C ($n = 5, 5, 5, 5$ at different temperatures), respectively.

Zygote period (0–0.8 h post-fertilization (hpf) at 23 °C, stage 1)

The zygote period (0–0.8 hpf at 23 °C) consisted of only one stage, stage 1, which lasted from fertilization to the end of the first mitotic cell division (Fig. 2). The initial mitotic division is shown in Fig. 2B, B'(optical section). Although narrowed, the cleavage furrow between the two daughter cells is not yet fully formed. The egg diameter was 180 ± 5 μm ($n = 10$).

Cleavage period (0.8–3 hpf, stages 2–9)

The cleavage period (0.8–3.0 hpf at 23 °C) consisted of eight stages, i.e., stages 2–9 (Figs. 2C, 3A). The cleavage

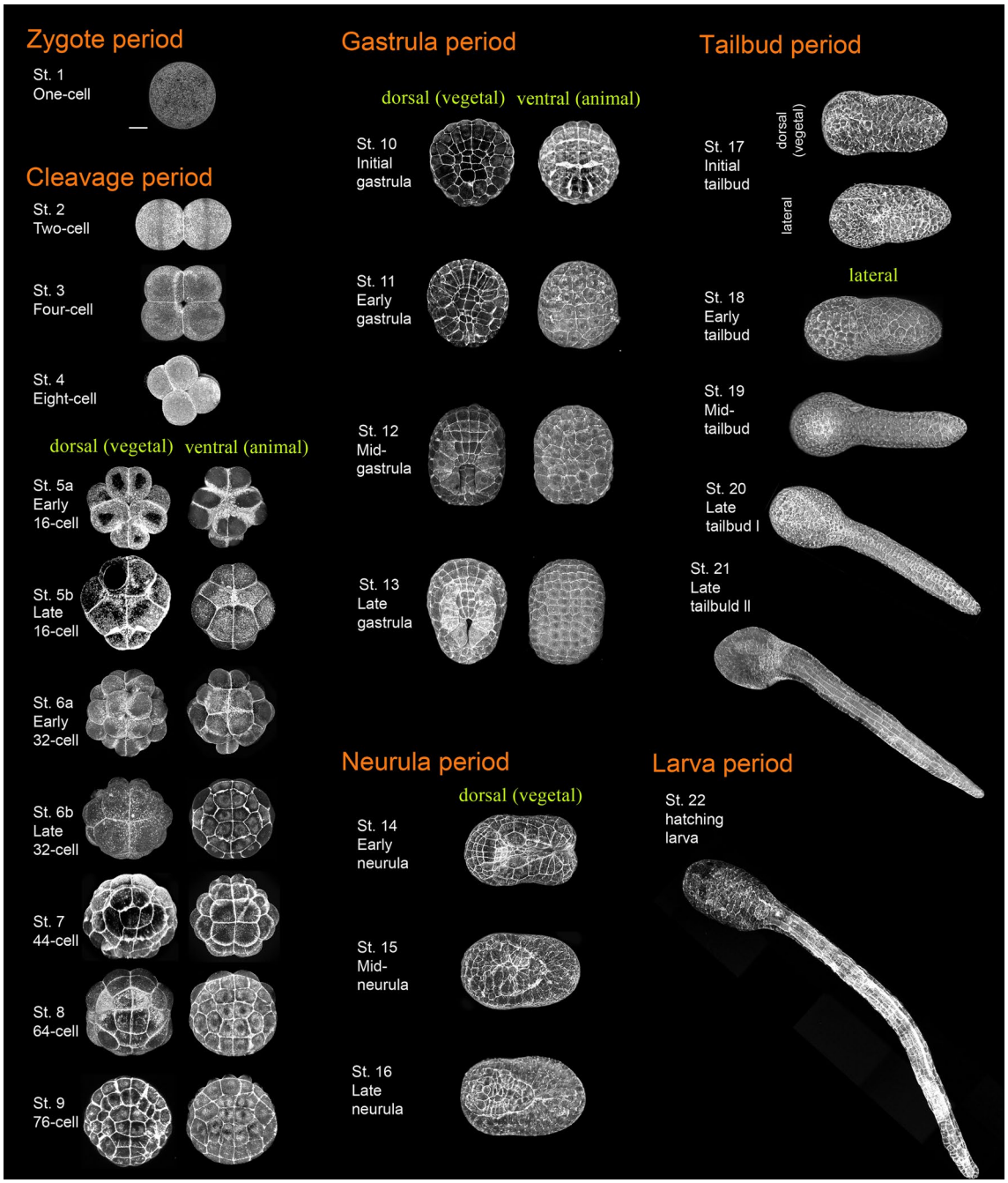

Fig. 1 Three-dimensional reconstructed images of *Styela clava* embryos in the developmental time course after fertilization. Fertilized eggs were dechorionated and incubated at 23 °C. F-actin of embryos were stained with Alexa Fluor™488 Phalloidin. Stage 1 is in the zygote period. Stages 2–9 are in the cleavage period. Stages 10–13 are in the gastrula period. Stages 14–16 are in the neurula period. Stages 17–21 are in the tailbud period. Stage 22 is in the larva period. In stages 1–13, the anterior side of each embryo is upward, and in stages 14–22, the anterior end is on the left. The criteria for each stage are shown in Table 3. Scale bar: 50 µm

stage was characterized by a sequence of mitotic divisions that culminated in the formation of numerous blastomeres. The embryos underwent seven divisions during this period and were bilaterally symmetrical. At the 16-cell stage, unequal cell division (UCD) occurred resulting in the formation of two smaller cells (Hibino et al. 1998). The asynchronous vegetative half split more quickly than the animal half following this stage, forming 32-, 44-, and 64-cell stages (McDougall et al. 2019). The developmental stages during this period were defined both by cell quantity and cell morphology. After each division of the blastomere contraction process (Supplementary Movies

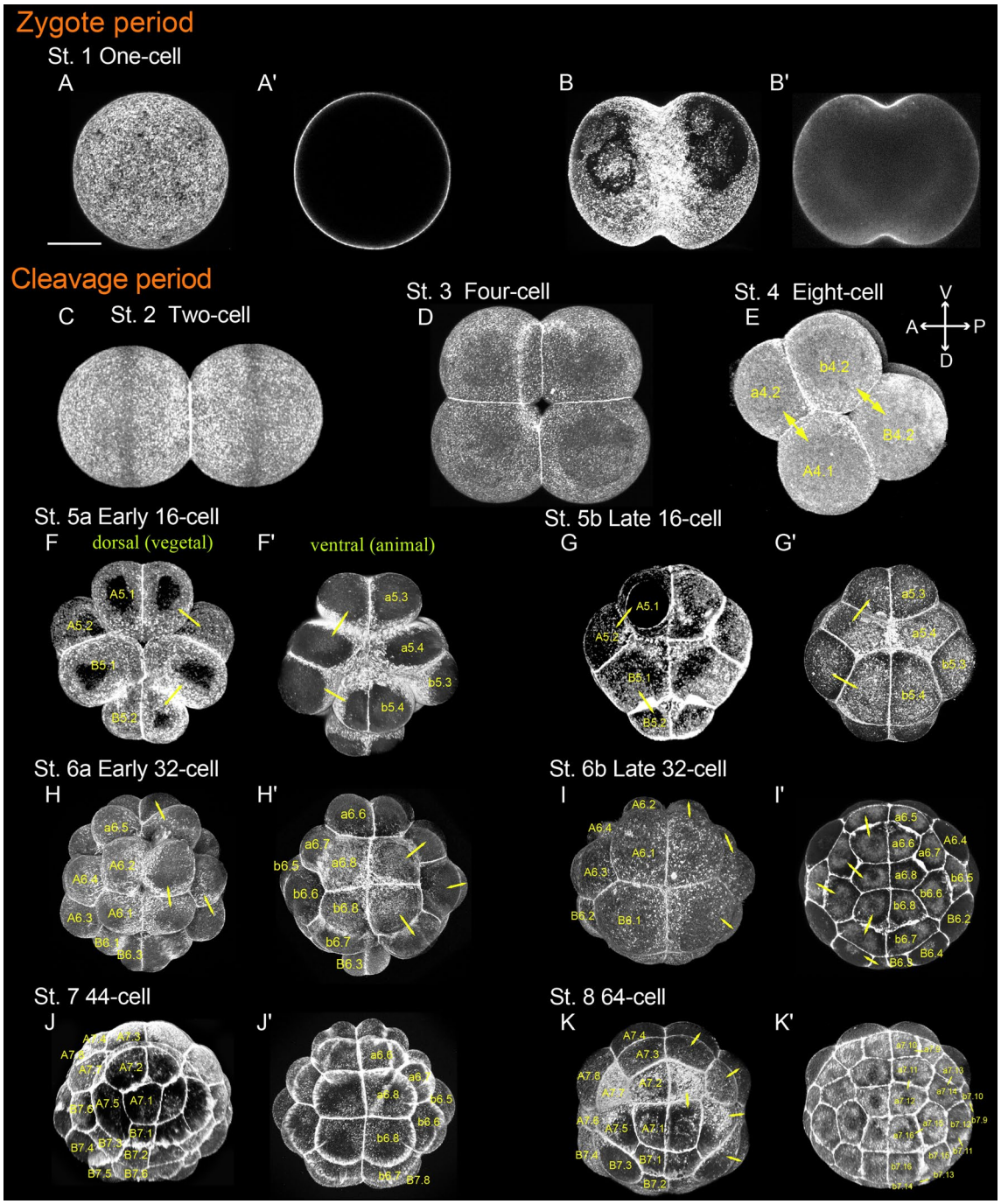

Fig. 2 *Styela clava* embryos at the zygote stage and for most of the cleavage period. Embryos are stained with Alexa Fluor™488 Phalloidin. Zygote period stage 1 (**A**–**B'**). 3D reconstructed images of embryos (**A**, **B**) and cross-sections (**A'**, **B'**). **A** Showing one cell. **B** Showing the first cell division. Cleavage period stage 2 to stage 8 (**C**–**K'**). **C**–**E** Showing a 3D reconstructed image without dorsoventral differentiation. 3D reconstructed images in dorsal view (**F**–**K**) and ventral veiw (**F'**–**K'**), respectively. Each blastomere was identified by the number of cell lineages; two headed arrows designate a pair of daughter cells. Anterior side of each embryo is upward unless otherwise specified. *A*, anterior, *D*, dorsal, *P*, posterior, and *V*, ventral, to show the orientation of the embryo. Scale bar: 50 µm

1, 2), the morphological changes were particularly obvious before and after the contraction of 16-cell and 32-cell stages. These two stages were further separated into two sub-stages.

Stage 2

Two-cell stage (0.8 hpf, Fig. 2C). The first cleavage plane is determined by the embryo dividing into the left and right halves.

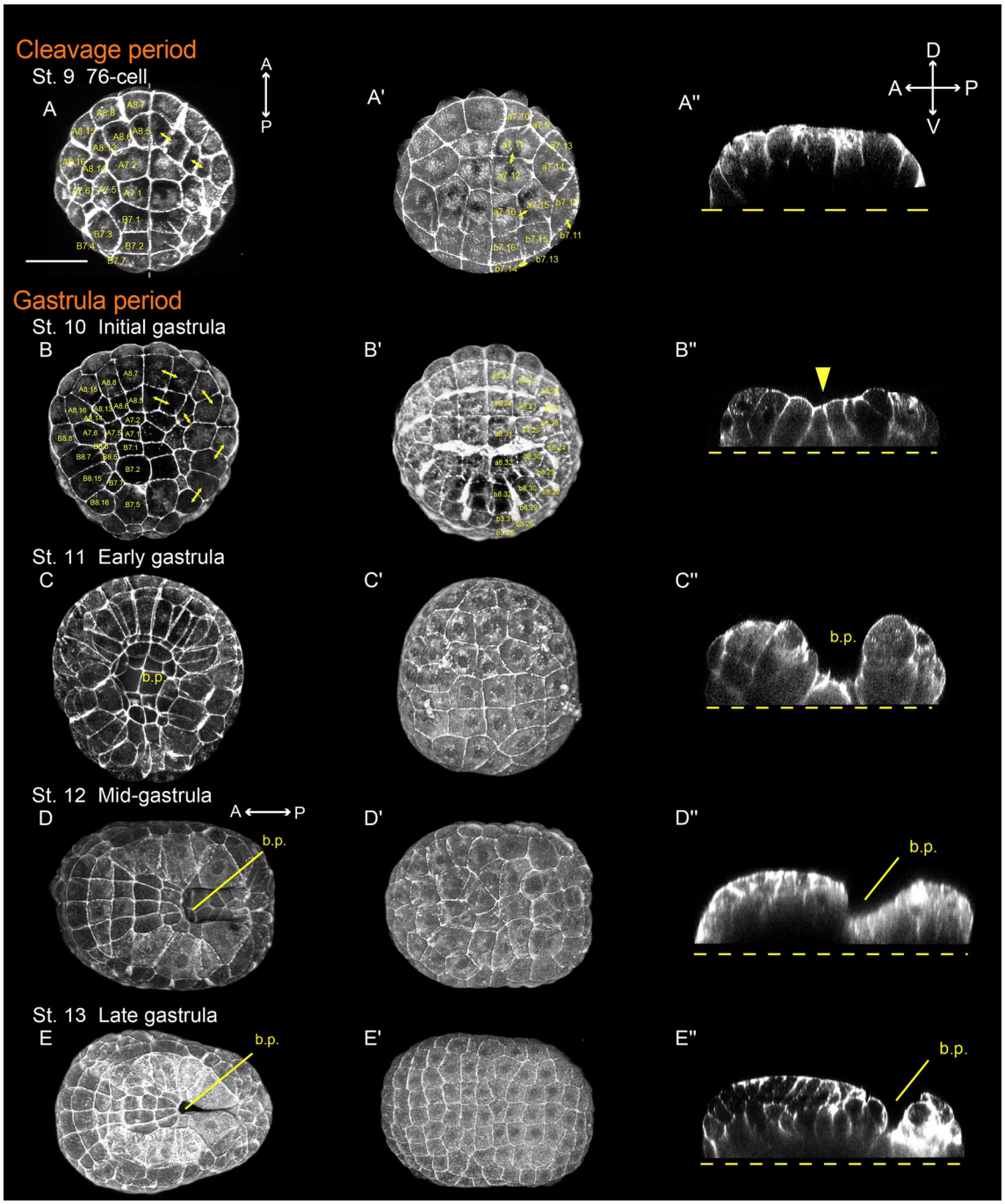

Fig. 3 *Styela clava* embryos at the cleavage and gastrula periods. Embryos were stained with Alexa Fluor™488 Phalloidin. The cleavage period stage 9 (**A**–**A”**) and the gastrula period stages 10–13 (**B**–**E”**). 3D reconstructed images of embryos in dorsal view (**A**–**E**), ventral view (**A’**–**E’**), and longitudinal section (**A”**–**E”**). **A, B** Each blastomere is indicated with the number of cell lineages; two headed arrows designate a pair of daughter cells. **A** Marked with obvious depressions (arrows). Anterior end of each embryo is upward in **A**–**C’** and on the left in **D**–**E’**. **A”**–**E”** Showing the orientation of the embryo, *A*, anterior, *D*, dorsal, *P*, posterior, and *V*, ventral. The positions of midline sections are indicated by dashed lines in **A”**–**E”**. *b.p.*, blastopore. Scale bar: 50 μm

Stage 3

Four-cell stage (1.2 hpf; Fig. 2D). The second cleavage plane is determined by the embryo dividing into anterior and posterior halves. Following cell division, each blastomere was initially arranged loosely with a gap in the center (Fig. 2D). Eventually, the blastomeres compacted and the gap was filled in.

Stage 4

Eight-cell stage (1.4 hpf; Fig. 2E). The embryo underwent a third cell division to separate the vegetal plane of the cell from the animal plane. These two planes were at a slight slanted angle and were not orthogonal. We used the nomenclature established by Conklin (1905b) to label the four founder cell lineages of *S. clava* as follows: a, animal anterior; b, animal posterior; A, vegetal anterior; B, vegetal posterior. Each blastomere in live embryos might be recognized based on its size (Fig. 2E, B4.2 blastomere is the largest). Eventually, embryo compaction occurred so that it resembled a sphere (Supplementary Movie 1, T = 1 h 17 min).

Stage 5

16-cell stage (1.6 hpf; Fig. 2F–G). All cells in both the vegetal and animal poles underwent a fourth cleavage. The embryo's distinct anterior–posterior polarity was apparent first and the B5.2 blastomere was much smaller than the others. In *C. robusta* and *Phallusia,* the occurrence of these phenomena is caused by the effect of the centrosome-attracting body (CAB) (Dumollard et al. 2017; Negishi et al. 2007). However, in *S. clava*, we were unable to observe this structure clearly using phalloidin staining. This stage was divided into two parts: an early, uncompacted 16-cell stage (stage 5a, Fig. 2F–F') and a late, compacted 16-cell stage (stage 5b, Fig. 2G–G').

Stage 6

32-cell stage (2.0 hpf; Fig. 2H–I). All blastomeres underwent a fifth cell division, which happened earlier in the vegetal than the animal lineages. The B5.2 division was once again asymmetric, resulting in a tiny posterior B6.3 cell. In *C. robusta*, this was caused by the CAB's effect, which was not observed in *S. clava*. This stage was divided into two parts: an early, uncompacted 32-cell stage which was almost spherical (stage 6a, Fig. 2H–H') and a late, compacted 32-cell stage which was flatter and had a bulging B6.2 cell (stage 6b, Fig. 2I–I').

Stage 7

44-cell stage (2.3 hpf; Fig. 2J). Only vegetal blastomeres underwent a sixth cell division during this stage. Bulging in vegetal blastomeres was observed.

Stage 8

64-cell stage (2.6 hpf; Fig. 2K). The animal blastomeres completed a sixth cell division. Due to the projection of the A7.8 and B7.4 blastomeres, the embryo appeared more angular than round when viewed from the animal pole.

Stage 9

76-cell stage (2.8 hpf; Fig. 3A). The vegetal half of the embryo had an asymmetrical pattern of cell division. Compared to animal cells, the vegetal blastomeres were taller and more columnar (Fig. 3A''). The vegetal side of the embryo became flattened and did not begin to sink until gastrulation was initiated. This stage was the last one prior to gastrulation.

Gastrula period (3–4 hpf, stages 10–13)

The gastrula period (3.0–4.0 hpf at 23 °C) consisted of four stages: stages 10–13 (Fig. 3B–E"). Gastrulation occurred at three stages between the sixth and seventh cleavages of the ascidian embryo. The initial stage is endoderm invagination, followed by mesoderm involution, and ultimately ectoderm epiboly (Swalla 1993).

Stage 10

Initial gastrula (3.0 hpf; Fig. 3B–B''). Gastrulation began with A7.1 blastomere apical constriction. The invagination in the middle of the vegetal pole was obvious in longitudinal sections (Fig. 3B", arrowhead).

Stage 11

Early gastrula stage (3.2 hpf; Fig. 3C–C"). The embryo developed into a cup-shaped structure as the endoderm cells progressively invaginated. When viewed from the vegetal aspect, the embryo was horseshoe-shaped.

Stage 12

Mid-gastrula stage (3.6 hpf; Fig. 3D–D"). The embryo's blastopore was still open in the middle. Six rows of cells—three rows of a-line cells (upper) and three rows of A-line cells (lower)—were arranged in a highly regular pattern on the flat neural plate.

Stage 13

Late gastrula stage (4.0 hpf; Fig. 3E–E"). The blastopore of the embryo was almost closed at the posterior end. The

embryo elongated anteriorly. Six or more rows of the neural plate formed, and the first two A-line neural rows (I and II near the blastopore) began to curve (start of neurulation).

Neurula period (4–4.8 hpf, stages 14–16)

The neurula period (4.0–4.8 hpf at 23 °C) consisted of three stages: stages 14–16 (Fig. 4A–C"). Neurulation is the transformation of a flat neuroectodermal sheet called the neural plate into a closed and extended neural tube (Nicol and Meinertzhagen 1988a, b). The neural tube then splits from the epidermis, forming the rudiments of the nervous system (Hashimoto et al. 2015).

Stage 14

Early neurula stage (4.0 hpf; Fig. 4A–A"). The a-line neural plate initially bent to form a furrow bordered by raised neural folds. The blastopore was completely closed. Zippering of neural tubes started from the posterior region of the embryo (Fig. 4A).

Stage 15

Mid-neurula stage (4.3 hpf; Fig. 4B–B"). The neural tube remained open. The neural plate of the A-line cells also caused a neural fold and the embryo was oval in shape (Fig. 4B).

Stage 16

Late neurula stage (4.6 hpf; Fig. 4C–C"). The neural tube closure commenced in the posterior area (Fig. 4C, arrowhead). The embryo elongated as the notochord precursors converged and intercalated.

Tailbud period (4.8–10 hpf, stages 17–21)

The tailbud period (4.8–10 hpf at 23 °C) consisted of five stages: stages 17–21 (Figs. 4D–D", 5A–D"'). The tailbud period was separated into four canonical stages: initial tailbud, early tailbud, mid-tailbud, and late tailbud. The late tailbud stage was divided into two sub-stages due to the prolonged development time and the significant morphological changes.

Stage 17

Initial tailbud stage (4.8 hpf; Fig. 4D–D). Separation between trunk and tail regions was present in embryos. The trunk and tail were equal in length. The neuropore migrated anteriorly, and the neural tube closure in the posterior area was nearly complete. Two rows of notochord cells were arranged in the left–right direction, some of which were still interdigitating and in the process of intercalation.

Stage 18

Early tailbud stage (5.2 hpf; Fig. 5A–A"). The neuropore had closed at the top of the trunk. Separation between tail and trunk regions was more distinct and the tail was significantly longer than the trunk (Tail/Trunk ratio = 1.2). Neurulation, and the intercalation of the few notochord cells that were positioned most anteriorly, were completed.

Stage 19

Mid-tailbud stage (5.9 hpf; Fig. 5B–B"). The length of the tail was 1.8 times that of the trunk (Table 3). The intercalation of notochord cells was completed. Viewed from the lateral aspect, the tail contained three rows of muscles on each side, with each medio-lateral line having seven muscles and each lateral line having four muscles. In general, a total of 36 muscle cells and 40 notochord cells were found in *S. clava* (see section mode of RAMNe).

Stage 20

Late tailbud stage I (7.0 hpf; Fig. 5C–C"). Pigmentation of the otoliths could be observed under an anatomical microscope (Supplementary Fig. S2). The length of the tail was 2.3 times longer that of the trunk.

Stage 21

Late tailbud stage II (8.0 hpf; Fig. 5D–D"). The length of the tail was four times that of the trunk. The epidermal cells in front of the trunk developed in a columnar fashion but did not protrude to form into palps. The notochord and muscle cells elongated along the A-P axis. Immediately prior to hatching, tail twitching was occasionally observed.

Larva period (10 hpf, stage 22)

Stage 22

Hatching larva (10.0 hpf at 23 °C, Fig. 6). The trunk grew longer and became more rectangular. The otoliths and ocellus could be observed under an anatomical microscope (Supplementary Fig. S3). Only one siphon primordium (either atrial or oral siphon primordium) was observed in the posterior region of the trunk.

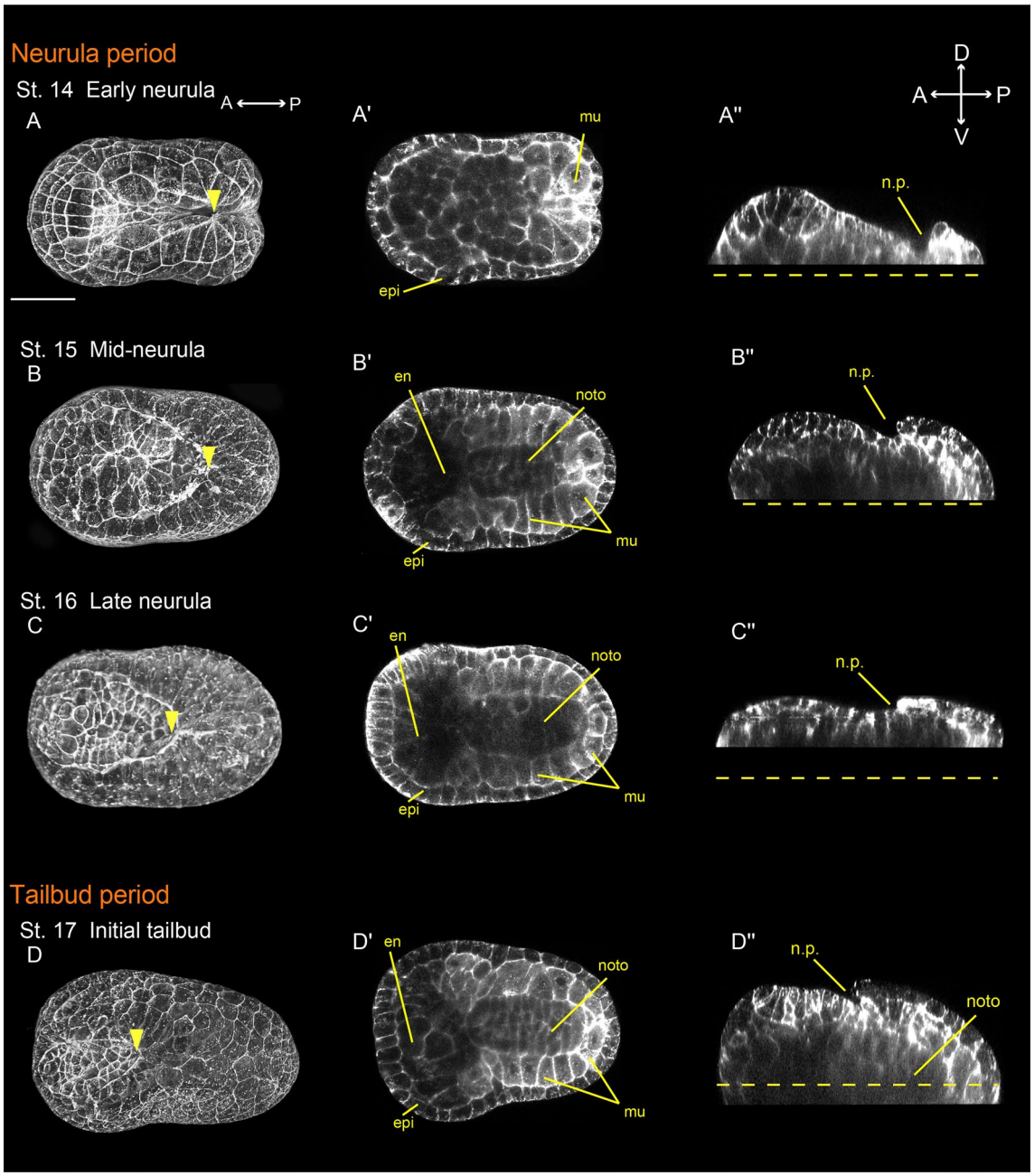

Fig. 4 *Styela clava* embryos at the neurula and tailbud periods. Embryos were stained with Alexa Fluor™488 Phalloidin. The neurula period is stages 14–16 (**A–C"**) and the tailbud period is stage 17 (**d–D"**). 3D reconstructed images of embryos in dorsal view (**A–E**), cross-section (**A'–D'**), and longitudinal section (**A"–D"**). Anterior end of each embryo is on the left (**A–D'**). **A"–D"** Showing the orientation of the embryo, *A*, anterior, *D*, dorsal, *P*, posterior, and *V*, ventral. The anterior edge of neural tube closure is indicated by arrowheads. The positions of midline sections are indicated by dashed lines in (**A"–D"**). *en*, endoderm; *epi*, epidermis; *mu*, muscle; *noto*, notochord; *n.p.*, neuropore. Scale bar: 50 μm

The unique processes in early development of *S. clava*

We observed sereval unique organogenesis events during early development of *S. clava*, including the processes of notochord formation, the disappearance of palps, and tail regression.

In ascidians, notochord tissue is the most significant tissue localized at the midline region of the tail. It provides mechanochemical signals and serves as a hydrostatic

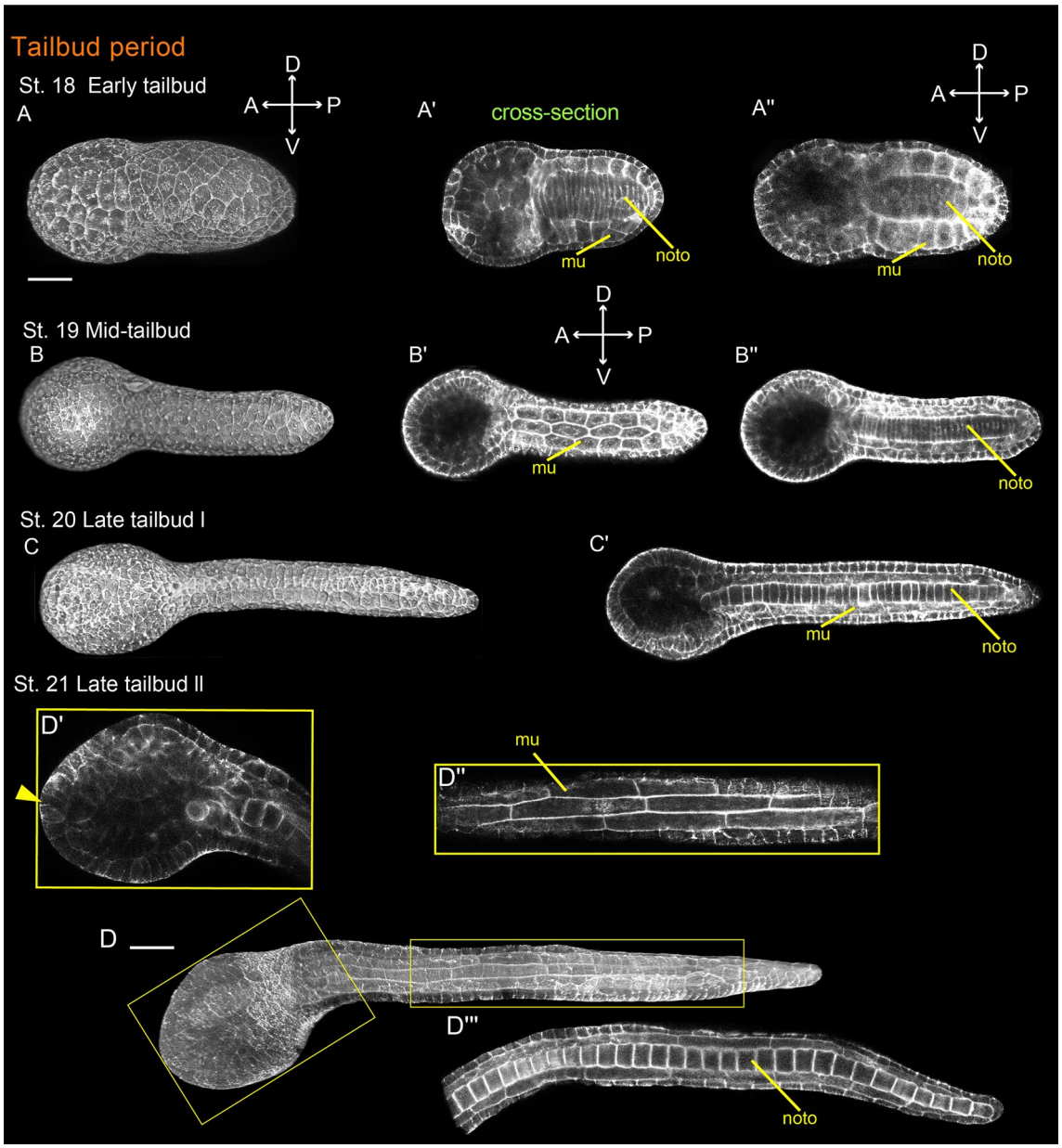

Fig. 5 *Styela clava* embryos at the tailbud period. Embryos were stained with Alexa Fluor™488 Phalloidin. The tailbud period is stages 18–21 (**A**–**C''**). 3D reconstructed images of embryos in lateral view (**A**–**E**) and longitudinal section (**B'**–**E'**, **A''**–**E''**). **A'** Cross-section, indicating incomplete notochord cell intercalation. **B'** is a shallower lateral section than **B''.** Enlarged longitudinal section of the trunk (**D'**) and tail **(D'', D'''): D''** is a shallower lateral section than **D'''**. Anterior end of each embryo is on the left. Embryo orientation is shown by *A*, anterior; *D*, dorsal; *P*, posterior; *V*, ventral; *mu*, muscle; *noto*, notochord. Scale bar: 50 μm

skeleton during embryogenesis and the hatching larva stage. The notochord organogenesis process can be separated into three main phases in *C. robusta* embryogenesis (Lu et al. 2019): cell intercalation, which leads to the notochord forming a single row of cells; cell elongation, which lengthens the notochord along the A-P axis; and tubulogenesis, which provides more flexibility and rigidity to notochord tissue (Mizotani et al. 2018; Peng et al. 2020; Zhao et al. 2021). *Ascidiella aspersa* also seems to go through all three stages based on the available data (Funakoshi et al. 2021). In contrast, we observed only the first two phases during embryogenesis in *S. clava*. The intercalation of notochord cells was completed during the initial tailbud to early tailbud stage. After the mid-tailbud stage, coin-like notochord cells were elongated along the A–P axis to form drum-shaped cells (Fig. 7A). However, no lumen structure was detected in

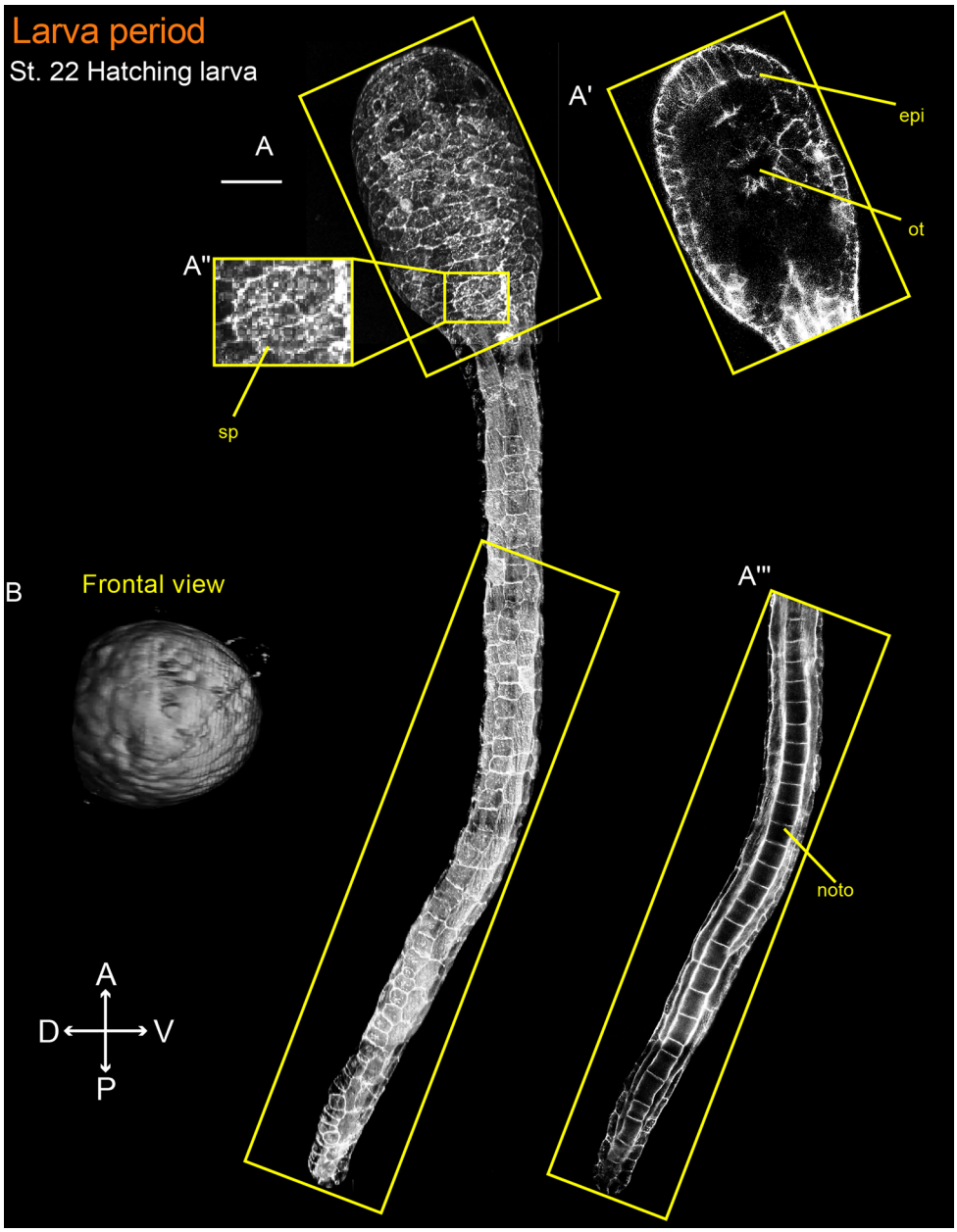

Fig. 6 *Styela clava* embryos at the hatching larva period. Embryos were stained with Alexa Fluor™488 Phalloidin. The hatching larva period is stage 22. **A** 3D reconstructed images of embryos in lateral view, showing the types of epidermal cell. **B** Longitudinal sections of trunk. **A'' '** Enlargement of trunk surface, revealing a siphon primordium. **A'''** Longitudinal sections of the tail. **B** Frontal views of the trunk in 3D reconstructed images, showing no protruding palps. Embryo orientation is shown by *A*, anterior; *D*, dorsal; *P*, posterior; *V*, ventral; *sp*, siphon primordium; *epi*, epidermis; *mu*, muscle; *noto*, notochord; *ot*, otolith; Scale bar: 50 µm

the notochord after cell elongation, even at the stage of tail regression initiation (Fig. 7A, hatching larva). These findings are not consistent with a previous study which reported luminization in *S. clava* (Jiang and Smith 2007). We also found that the embryos and larvae of *S. clava* did not form palps. In *C. robusta* and *A. aspersa* (Funakoshi et al. 2021), the anterior-most ectoderm cells thicken and protrude into three palps at the front of the nerve plate. The palps are involved in larval attachment and metamorphosis, and function in both chemo- and mechano-sensation (Wagner et al. 2014; Wakai et al. 2021). From the late tailbud stage to the hatching larva stage, we performed a 3D reconstruction of the trunk and confirmed that no protruding structures are present on the top of the trunk in *S. clava* embryos and larvae (Fig. 7B, yellow arrowhead). However, a thickening of the anterior ectoderm cells was detected from the late tailbud II stage (Fig. 5D', arrowhead).

Another obviously distinct developmental characteristic of *S. clava* larvae is tail regression. The tail regression

process appears to differ greatly among ascidians (Cloney 1982). The time duration of tail regression and how the tail tissue is arranged in the trunk are the two key differences. *Styela clava* larval tail regression started at 3 hph and took only about 15 min to complete at 23 °C (from tail regression initiation to tail completely regressed into the trunk), while *C. robusta* larval tail regression starts at 12 hph and takes more than one hour to complete at 18 °C (Matsunobu and Sasakura 2015). Furthermore, the arrangement of the regressed-tail tissue in the trunk differs significantly between *S. clava* and *C. robusta*. The notochord cells of *S. clava* were concentrated in the posterior part of the trunk part and were completely seperated from other regressed-tail tissues; muscle cells rapidly buckled into a spherical shape and were scattered along the edge of the posterior part of the trunk; the trunk tissue was compressed into the anterior part of the trunk (Fig. 7C, left). In contrast, the internal tissues of *C. robusta's* tail were stacked in a coiled form, called coiled internal tissues (IT) (Yamaji et al. 2020), and the muscle and notochord tissues were spirally arranged in the posterior part of the trunk with no obvious cell buckling or tissue reconstruction (Fig. 7C, right).

The present study also revealed notable differences among *S. clava, C. robusta*, and *A. aspersa*. We found only one siphon primordium (either atrial or oral) at the posterior end of the trunk in *S. clava* larvae (Fig. 6A, A"), whereas there are two atrial siphon primordia in *C. intestinalis* and *A. aspersa* larvae (Funakoshi et al. 2021; Hotta et al. 2007). We also compared the ratio of the tail-to-trunk length among the three species and found that *C. robusta* had the highest, followed by *S. clava*, and *A. aspersa* (Table 4). Among these three ascidians, a decrease in the ratio of tail-to-trunk length was observed only in *S. clava.* This occurred at the hatching larva stage and was caused by an increase in trunk length. Moreover, we also compared the number of lateral epidermal cells in the tail of the three species and found that *C. robusta* had the highest number, i.e., ~ 60 cells (Hotta et al. 2007), *A. aspersa* had the lowest, i.e., ~ 40 cells (Funakoshi et al. 2021), while *S. clava* has a middle number, i.e., ~ 50 cells. Furthermore, from stage 18 to stage 20, there was no significant ventral bending of the tail in dechorionated *S. clava* embryos (Fig. 5A–C), whereas such bending is present in both *C. robusta* and *A. aspersa* embryos (Funakoshi et al. 2021; Hotta et al. 2007; Kogure et al. 2022; Lu et al. 2020). It is noteworthy, however, that dechorionation might have had an effect on the developmental potential of embryos at the tailbud stages.

Resources of *S. clava* morphology for network-based research

We integrated the raw data of *S. clava* into a web-based database, "RAMNe." The images were exported as a series of files to enable easy viewing of cross-sectional and 3D images using a web browser (Fig. 8, https://chordate.bpni.bio.keio.ac.jp/RAMNe/latest/index_styela.html). At the web interface of the developmental table, images were linked to information on developmental stages, developmental nomenclature, hour post-fertilization (hpf), % hatch, cell lineage, and time-lapse movies. Additionally, 3D reconstruction images, cross-sectional images, and DIC images of the embryos are also displayed (Fig. 8A). Users can interactively view 3D images (Fig. 8B) and z-section images (Fig. 8C) online by selecting any developmental stage from the table. Furthermore, the database also displays corresponding images from *C. robusta* and *A. aspersa* (Funakoshi et al. 2021; Hotta et al. 2007, 2020), which can easily be compared with *S. clava* (Fig. 8D). The detailed usage of the RAMNe database has been described previously (Funakoshi et al. 2021).

The transgene method optimization and protocols

The eggs of *S. clava* are difficult to dechorionate due to their thick and dense chorions. These structures primarily comprise covered cylindrical box-like follicular cells on the outside and test cells dispersed irregularly on the inside, similar to *Styela plicata* eggs (Villa and Patricolo 2000). To establish the ideal dechorionation method, we first tested enzymes (chitosan, chitinase, and NaClO) and other components of the dechorionation solution used in *C. robusta*, such as altering the amounts of NaOH and sodium thioglycolate (see Table 1). Our results showed that the dechorionation solution with chitosan or chitinase cannot remove the chorion within 30 min; using NaClO caused destruction of the oocyte; and increasing the concentration of NaOH and sodium thioglycolate did not significantly reduce dechorionation duration, but the embryos were more susceptible to malformation. The optimum dechorionation solution for *S. clava* was found to be 1% sodium thioglycolate, 0.05% proteinase E, 55 µL 10 N NaOH, and 10 mL filtered seawater (FSW). Compared with the dechorionation method for *C. robusta* embryos, extra NaOH (55 µL) needed to be added to the dechorionation solution, while the concentration of protease E and sodium thioglycolate remained unchanged. Furthermore, a longer dechorionation time duration (18 min) was necessary to totally remove the chorion for *S. clava* embryos. Based on the above experimental results, we developed a standard protocol for *S. clava* embryo dechorionation. The feritilized eggs were immersed in the dechorionation solution (Fig. 9A, step 1) and, by gently pepetting for around 18 min, the chorion can be removed (Fig. 9A, step 2). Dechorionated eggs were then washed five times with FSW

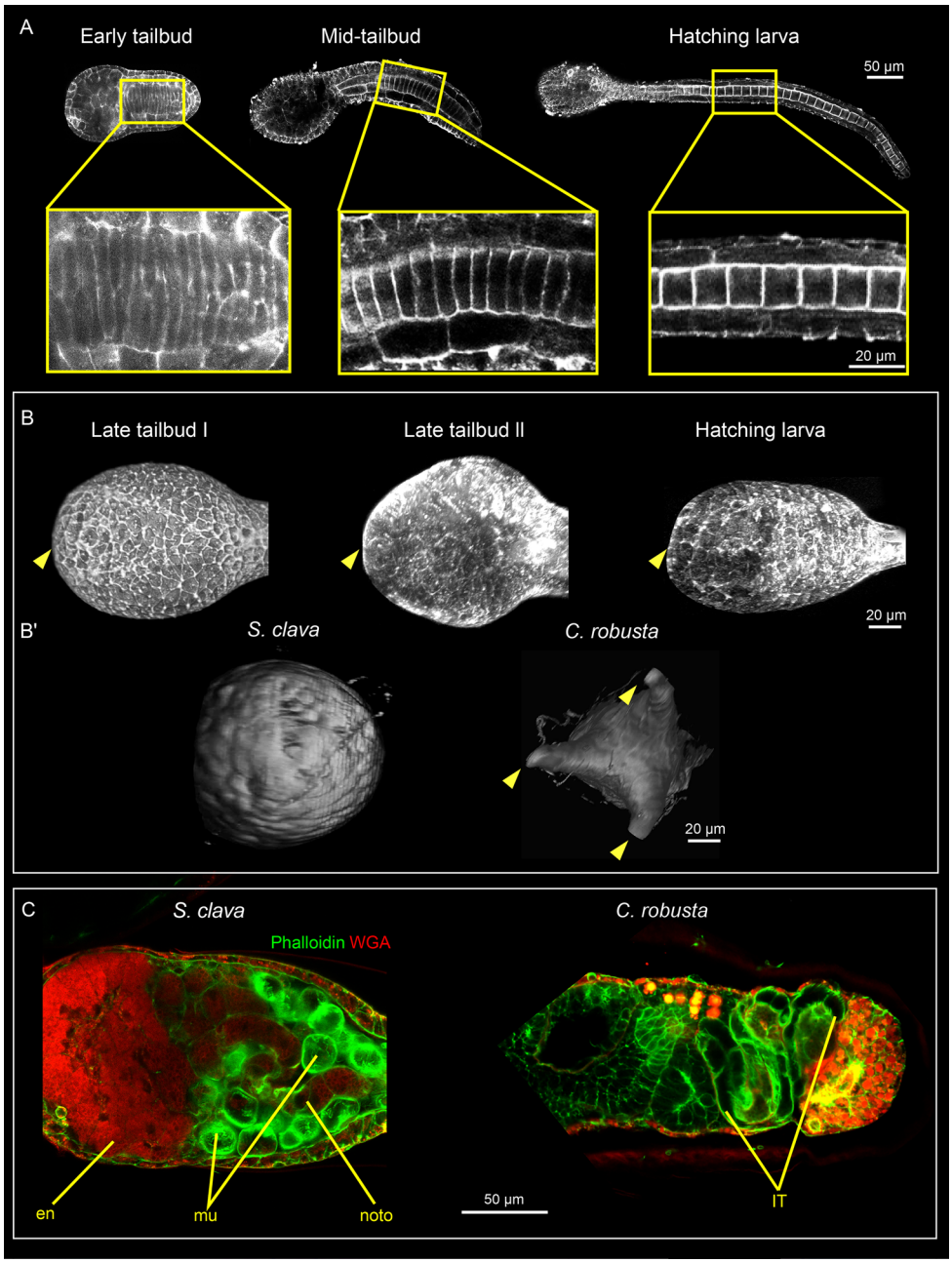

Fig. 7 Comparison of developmental processes in *Styela clava*, *Ciona robusta*, and *Ascidiella aspersa*. Embryos were stained with Alexa Fluor™488 Phalloidin and Alexa Fluor™555 WGA (ThermoFisher, W32464). **A** Longitudinal sections and corresponding enlarged views of embryos in different stages (from left to right: early tailbud, mid-tailbud, and hatching larva stage). **B** 3D reconstructed images of half-frontal views of the trunk in three stages showing no palps were formed (arrows). **B'** 3D reconstructed images of frontal view of the trunk at hatching larva stage (left: *S. clava*; right: *C. robusta*) showing no palps were formed in *S. clava*, whereas three palps are visible in *C. robusta* (indicated by arrows). **C** Longitudinal sections of the trunk in tail regression stage (left: *S. clava*; right: *C. robusta*). The notochord cells of *S. clava* are tubular with WGA signals on the inside (red), and the muscle cells are curled with only phalloidin signals (green). In contrast, the notochord and muscular cells of *C. robusta* are coiled and stacked in the trunk, forming a structure known as the internal coiling tissue (*IT*). *en*, endoderm; *mu*, muscle; *noto*, notochord

and transfered into an agarose-coated dish. To avoid harm and aberrant development due to the dechorionation solution, the dechorionation process must be completed within 18 min. The dechorionated eggs could either be used for the subsequent electroporation process or incubated for morphological observation.

Subsequently, we explored the optimum transgene technology in *S. clava* by electroporation. By using the Gene Pulser Xcell System (BIO-RAD, Hercules, USA), we optimized the electroporation-related parameters, including electroporation voltage, capacitance, and plasmid concentration. The initial voltage value was calculated from the size of the egg, and the specific formula was as follows (Zeller 2018):

$$E_c = \frac{V_c}{0.75 \times d_{\text{cell}}},$$

where E_c is the critical field strength in volts per centimeter, V_c is the membrane permeation voltage (1 at 20 °C) and d_{cell} is the cell diameter in centimeters (Multiporator manual, www.eppendorf.com). The diameter of *S. clava* eggs was 180 ± 5 μm ($n = 10$) and, together with our experimental

quantification on the survival rate after electroporation, the optimal voltage value was 45 V (see Table 2). After determining the voltage, we searched for the ideal value of capacitance. A previous study showed that higher capacitance values improved transfection but reduced viability (Zeller 2018). Capacitances ranging from 1500 to 3000 μF were investigated and it was found that 2000 and 2500 μF was suitable for electroporation. We also found that a higher concentration of plasmid DNA was necessary for high transgene efficiency. Thus, we established a standard protocal for *S. clava* embryo electroporation, which resulted in an electroporation efficiency of 37.2 ± 9.7%. In brief, dechorionated fertilized eggs (300 μL) were mixed with 80 μg plasmid DNA in a prefabricated electrotransfer solution (0.77 mol/L mannitol in ddH_2O). Then, the mixture was transfered into 4 mm cuvettes with a Gene Pulser Xcell System (BIO-RAD) and electroporated with expontential decay pulse. Electroporated eggs were recovered for around 10 min, washed once, transferred into an agarose-coated dish (Fig. 9B) and incubated at 18 °C.

Labeling cells with a tissue-specific driver in *S. clava* embryos

We next attempted to introduce exogenous plasmids into fertilized eggs of *S. clava*. We designed a tissue-specific fluorescent fusion construct to specifically label the tissue cells. The upstream 3 kb of the *C. robusta* homologous genes *MA1* and *Epi1* (Chiba et al. 1998) were used as the driver to force a GFP or tdTomato fluorescent reporter to be expressed in specific tissue cells (Fig. 9C). After electroporation of these constructs, the results showed that the *Sc-Ma1 > eGFP* plasmid was expressed in tail muscle cells (Fig. 9D), whereas the *Sc-Epi1 > tdTomato* plasmid was expressed in the epidermal cells (Fig. 9E). Due to the mosaic expression in ascidians, the constructs were only expressed in part of the target tissue cells. The fluorescently labeled embryos could develp into larval stages in our experiments, by which the subcellular location of proteins could be visualized in a living embryo to track the dynamics of this protein.

Discussion

In this study, we developed a chemical method that can easily remove the chorionic membrane from the eggs of *S. clava*, allowing us to observe the early embryogenesis easily and offer the possibility to genetically manuplate the eggs. Based on this technique, we established a developmental atlas of *S. clava* and defined the developmental stages for this species for the first time. Combining CLSM, DIC, and time-lapse imaging, the internal and exterior structures of the embryo at each stage and time of development were meticulously documented. We accurately depicted the anatomy and developmental stages of *S. clava* and established a standard developmental table, which enables detailed comparison of tissue morphology and differentiation between wild-type embryos and knockout mutant embryos. The processes of embryogenesis and quantitative data of *S. clava* are summarized in Table 3, including the developmental duration, basic embryonic morphological characteristics, time ratio to hatch, and tail-to-trunk length ratios. We also compared the tail-to-trunk length ratios and tail length with *C. robusta* and *A. aspersa* (Table 4). Additionally, based on the mature electroporation technique in *C. robusta*, we applied the electroporation technique in *S. clava* for the first time. DNA constructs were successfully introduced into *S. clava* fertilized eggs. These new techniques, and the developmental atlas of *S. clava* embryos and larvae, provide a crucial basis for *S. clava* to be used as a marine model organism for reserach on developmental biology, evo-devo, ecology, and cell biology.

Styela clava is a potential model organism for studying morphological changes such as tail retraction during metamorphosis. Additionally, notochord development in *S. clava* embryos was straightforward during the tailbud period and did not involve vacuolation to generate the lumen, making it an ideal model for research on intercellular insertion and polarity establishment. However, it is noteworthy that dechorionation has been found to have a slight impact on morphogenesis (Oonuma et al. 2016; Kourakis et al. 2021). Nevertheless, based on the present findings, we expect chorionated specimens of *S. clava* to be used in future research on developmental processes.

It has been reported that the leathery sea squirt ascidian *S. clava* is an invasive species that shows high capacity for environmental adaptation and tolerance to temperature and salinity (Dupont et al. 2009; Goldstien et al. 2010; Locke et al. 2007). The results of studies on transcription factors and chromosome-level gene expression in *S. clava* have revealed a significant increase in the number of transposons and heat shock protein-related genes (Wei et al. 2020). These findings shed light on the organism's environmental adaptation mechanisms based on its genome and molecular networks. However, experimental validation and detailed molecular mechanisms are impossible without transgenic manuplation. Based on the dechornation and electroporation tenniques reported here, transgenic technologies, such as gene knockout and overexpression, could easily be applied in *S. clava*. This would significantly improve the operability of embryonic genes, shedding a powerful new light on the molecular mechanisms of the development of invasive ascidians and chordates.

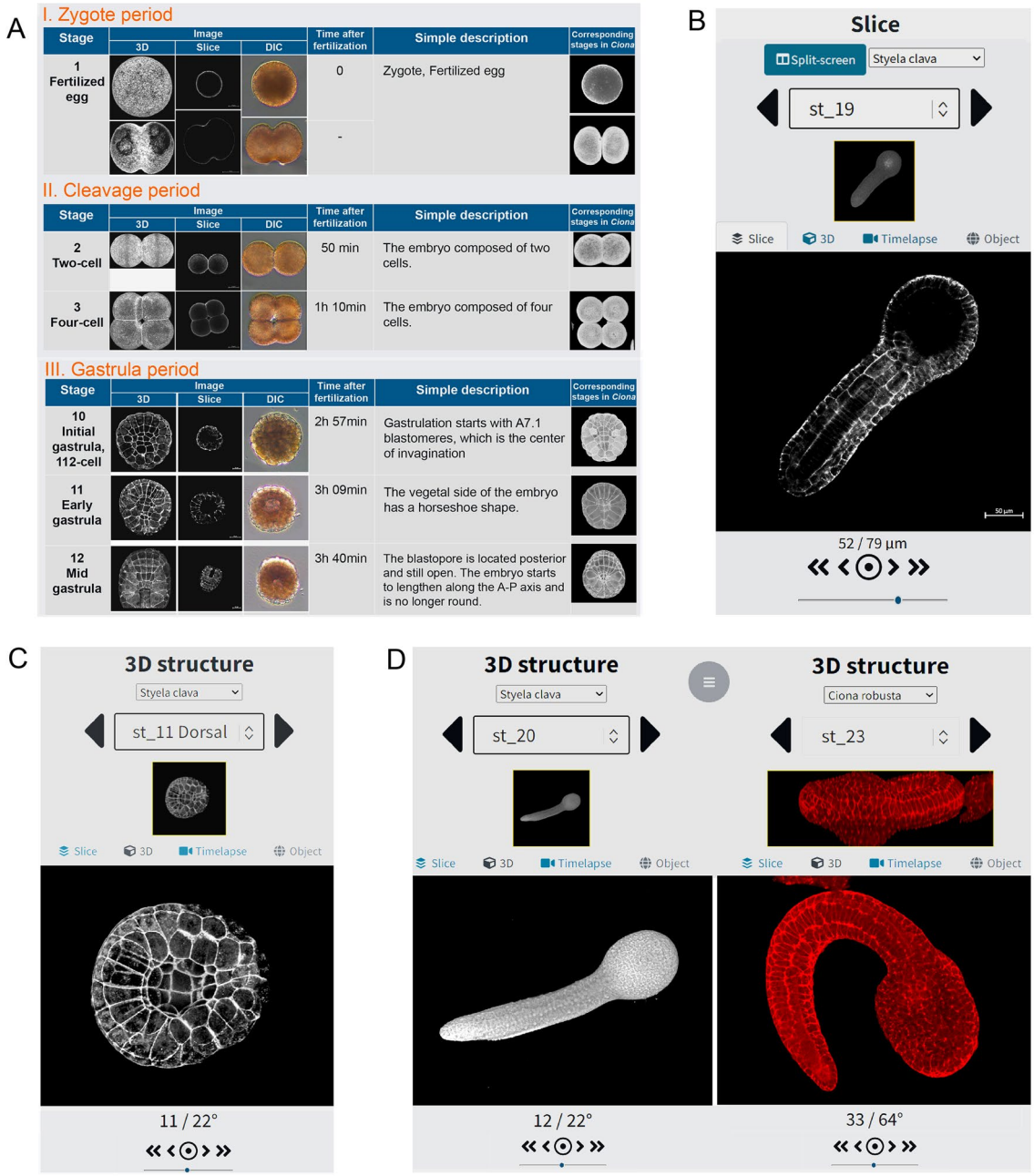

Fig. 8 Screenshot of the database. To use the database, please refer to the website: https://chordate.bpni.bio.keio.ac.jp/RAMNe/latest/index_styela.html. **A** "Developmental table" refers to the two-dimensional images from a fertilized egg to the hatched larva as viewed by CLSM using an inverted microscope. **B** Information about section images. **C** Information about 3D images. **D** "Dual display mode" can display and compare the images of *S. clava* to *C. robusta* and *A. aspersa* (Funakoshi et al. 2021; Hotta et al. 2007, 2020) interactively

Materials and methods

Animal collection and fertilization

Adults of *S. clava* (Herdman, 1881) were collected from Weihai City, China, and acclimated into seawater at 18 °C under constant light to accumulate gametes in the laboratory. The 18S rRNA gene was amplified and the PCR products were sequenced for species identification (Wei et al. 2020). The adult animals were dissected, and the mature eggs and sperm were isolated from the gonoducts from different individuals. A drop of 1 mol/L Tris pH 9.5 (Kobayashi and Satou 2018) was added to activate the sperm which was

Table 1 The effects of different dechorionation solution components on chorion removal in *S. clava*

Different Enzyme	Chitosan[a]		NaClO[b]		Proteinase E[c]				
Dechorionation solution components	Chitosan	2 mL	NaClO	0.05 mL or 0.1 mL	Proteinase E	0.05%			
	Acetic acid	0.2 mL	FSW	Up to 10 mL	Sodium thioglycolate	1%	1%	1.5%	1%
	FSW	10 mL			10N NaOH (μL)	48	55	55	60
					FSW	Up to 10 mL			
Dechorionation duration (min)	> 30 min		< 6 min			20	18	19.5	17.5
Dechorionation efficiency	Chorions unremovable		Oocytes destructed			×	√	×	×

Using chitosan[a] for over 30 min failed to remove the chorions. Using NaClO[b], the oocytes were destroyed before the chorions. Using different concentrations of NaOH and sodium thioglycolate[c], the dechorionation time did not alter significantly and abnormalities of embryos were more likely to arise

then mixed with eggs at room temperature for 15–20 min. Fertilized eggs were washed with seawater through a nylon filter to remove sperm and debris and incubated in FSW at 16 ~ 23 °C.

The dechorionation approach of *S. clava*

The chorion provides protection to eggs, promotes fertilization, and prevents self-fertilization and polyspermism (Villa and Patricolo 2000). Additionally, we found that eggs without the chorion cannot be fertilized. Therefore, unless needed for specific experimental purposes, we typically removed the chorion after fertilization. Fertilized eggs were washed with FSW to remove impurities and sperm, and were then transferred to a 60 mm 0.1% agarose-coated dish with dechorionation solution. The chorions can be adequately digested by the enzyme after 18 min of blowing the eggs evenly using the dropper. Eggs might be blown violently for the first 10 min, and then carefully and gently during the next 8 min. A dissecting microscope was required to examine the proportion of dechorionated eggs. When the chorions of the majority of eggs (~ 80%) were removed, the dechorionated eggs were concentrated by gently swirling the dish to gather them in the center. They were then transferred to an agarose-coated dish and washed with FSW five times to clean the residual dechorionation solution. The dechorionated eggs were used either for incubation or electrical transfer.

The electroporation process

Using a pipette, 300 μL of seawater with the required amount of dechorionated eggs was transferred into a 1.5 mL tube holding 80 μL of ddH_2O, 80 μg plasmid DNA and 420 μL of electrotransfer solution (electroporation solution: 6.3 g mannitol, 5 mL FSW, and 45 mL ddH_2O). The solution was then gently mixed and transferred into a cuvette, which was placed in a holder. After electroporation with suitable parameters (45 V voltage, 2000–2500 μF capacitance, and 4 mm electrode cuvette width), the sample was gently transferred into a 90 mm 0.1% agarose-coated dish with FSW and incubated for about 10 min. Gently swirlling the dish enabled the eggs to be concentrated in the center and transferred into a new dish. The embryos were then allowed to develop at 18 °C.

Construction of tissue-specific fluorescent labeling clones

Two types of tissue-specific genes of *S. clava* were obtained from homologous *Epi1* and *MA1* genes (Chiba et al. 1998) in *Ciona*. The upstream 3 kb promoters of these were amplified from the genome of *S. clava* by polymerase chain reaction (PCR) with Phanta® Max Super-Fidelity DNA Polymerase (Vazyme, P505-d1). The vectors without promoters were reverse-amplified from fluorescent protein clones pEGFP or tdTomato with an identical polymerase. After purification by electrophoresis, the promoter recombined with one fluorescent protein vector, i.e., pEGFP or ptdTomato, by homologous recombination (Vazyme ClonExpress® II One Step Cloning Kit, C112-01) to create a tissue-specific fluorescent labeling clone. The primers and templates used are presented in Supplementary Table S2. The expression clones were sequenced with the primers shown in Supplementary Table S2 and promoter transfection efficiency was verified by electroporation.

Time-lapse imaging by inverted microscope

Time-lapse imaging movies from zygote development to swimming larva after dechorionation were taken using differential interference contrast (DIC) microscopy (OLYMPUS IX73). The room temperature was maintained at 23 °C by an air conditioner and the images were acquired every 1–3 min.

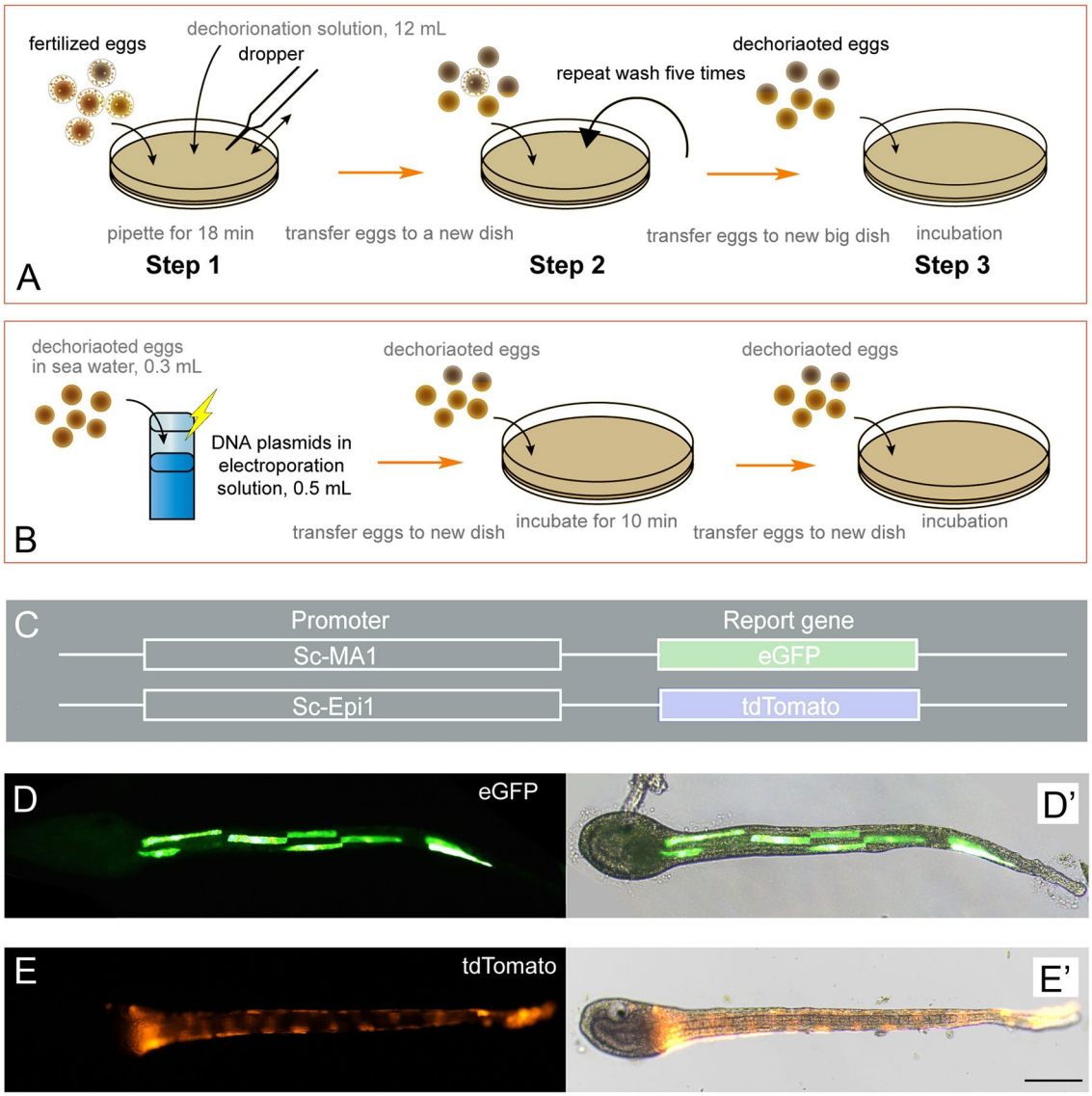

Fig. 9 *Styela clava* muscle and epidermal cells were labeled by electroporating expression clones with distinct fluorescent protein tags. **A**, **B** An illustration of the process for dechorionation (**A**) and electroporation (**B**). **C** Two types of tissue-specific promoters fusing with fluorescent gene vectors. **D** Larva inducing the Sc-Ma1 > EGFP vector expressing green fluorescent protein (GFP) in muscle cells. **E** Larva inducing the Sc-Epi1 > tdTomato vector labeled with tdTomato in epidermal cells. **D'–E'** Showing merged images with bright field and fluorescence microscopy. Anterior is to the left. Scale bars: 50 μm

Table 2 The effects of different voltage and capacitance on electroporation

Voltage	Different voltage				Different capacitance		
	60 V	50 V	45 V	40 V	45 V	45 V	45 V
Capacitance	2500/2000 μF	2500/2000 μF	2500/2000 μF	2500/2000 μF	3000 μF	2500/2000 μF	1500 μF
Transfection efficiency	×[a]	√	√	×	√	√	×
Normal development	×	×	√	√	×	√	√

Using higher voltage values improved transfection efficiency but damaged the egg in identical capacitance conditions. We were unable to determine plasmid transfection at 60 V ([a]) since the eggs were entirely broken and undeveloped. Under the same voltage condition, similarly, higher capacitance values improved transfection but reduced viability

Table 3 Stages of early embryonic development of *Styela clava* at 23 °C

Stage		Characteristics	Measurement of embryos		
			Time after fertilization	% Hatch	Tail/trunk ratio
I. Zygote period (0–0.8 h)					
St. 1	One cell	Zygote, the fertilized egg	0	0%	
II. Cleavage period (0.8–3 h)					
St. 2	Two-cell	The embryo is composed of two cells	50 min	9%	
St. 3	Four-cell	The embryo is composed of four cells	1 h 10 min	12%	
St. 4	Eight-cell	The embryo is composed of eight cells	1 h 24 min	14%	
St. 5a	Early 16-cell	The embryo is composed of 16 cells, Blastomeres are uncompacted	1 h 40 min	17%	
St. 5b	Late 16-cell	The embryo is composed of 16 cells, Blastomeres have been compacted	1 h 55 min	20%	
St. 6a	Early 32-cell	The embryo is composed of 32 cells, Blastomeres are uncompacted	2 h 03 min	21%	
St. 6b	Late 32-cell	The embryo is composed of 32 cells, Blastomeres have been compacted	2 h 12 min	23%	
St. 7	44-cell	The embryo is composed of 44 cells. Bulging in vegetal blastomeres	2 h 21 min	24%	
St. 8	64-cell	The embryo is composed of 64 cells	2 h 36 min	27%	
St. 9	76-cell	The embryo is composed of 76 cells. Planarization on its vegetal side in preparation for gastrulation	2 h 47 min	29%	
III. Gastrula period (3–4 h)					
St. 10	Initial gastrula	Gastrulation starts with the apical constriction of A7.1 blastomeres, which is the center of invagination	2 h 57 min	30%	
St. 11	Early gastrula	The vegetal side of the embryo has a horseshoe shape	3 h 09 min	32%	
St. 12	Mid-gastrula	The blastopore is located posteriorly and is still open. The embryo starts to lengthen along the a-p axis and is no longer spherical	3 h 40 min	38%	
St. 13	Late gastrula	The blastopore is located posteriorly and is nearly closed	3 h 57 min	41%	
IV. Neurula period (4–4.8 h)					
St. 14	Early neurula	Neural plate forms a furrow. The blastopore is completely closed	4 h 04 min	42%	
St. 15	Mid-neurula	The embryo has an oval shape. A-line cells create a neural fold	4 h 20 min	45%	
St. 16	Late neurula	The neural tube closure starts in the posterior part	4 h 37 min	48%	0.9
V. Tailbud period (4.8–10 h)					
St. 17	Initial tailbud	First indication of a separation between trunk and tail parts in this stage	4 h 47 min	49%	1.0
St. 18	Early tailbud	A few anterior notochord cells finish intercalation and the neuropore has just closed	5 h 10 min	53%	1.4
St. 19	Mid-tailbud	Intercalation of the notochord cells is completed. Tail twice as long as trunk	5 h 52 min	60%	1.9
St. 20	Late tailbud I	The pigmentation of the otolith starts	7 h 07 min	73%	2.3
St. 21	Late tailbud II	On the verge of hatching. Tail four times as long as trunk	9 h 06 min	88%	4.3
VI. Larva period (10 h)					
St. 22	Hatching larva	Hatching. Swimming instantly. The trunk has an elongated rectangular shape	9 h 43 min	100%	3.5

A total of 22 stages were divided into six periods. Columns from left to right: "Characteristics" were primarily based on observations of specimens under a dissecting microscope. "Measurement of embryos": Time after fertilization (23 °C, $n=5$), % hatch = rate of T (min)/583 (min), and ratio of tail/trunk length

Fixed embryo image collection by confocal laser scanning microscopy

Confocal images were taken with a ZEISS confocal laser scanning microscope (CLSM) equipped with 20X (Numerical aperture: 0.75) and 63X oil immersion objectives (NA: 1.4). Z-series images were taken at intervals of 0.8–1 μm, resulting in stacks of 80–100 images. Image analysis and 3D reconstruction were performed with ZEISS software packages. Some of the lengthier embryos

Table 4 Tail/trunk ratio and Tail/trunk length of *Styela clava*, *Ciona robusta* and *Ascidiella aspersa*

Stage		*Styela clava*			*Ciona robusta*				*Ascidiella aspersa*
		Tail/trunkratio	Trunk length (μm)	Tail Length (μm)	Corresponding stage	Tail/trunk ratio	Trunk length (μm)	Tail Length (μm)	Tail/ trunk ratio
St. 16	Late neurula	0.9	100.3 ± 3.1	98.1 ± 10.4	St. 16	1.0	85.3	84.2	
St. 17	Initial tailbud	1.0	98.0 ± 1.8	105.6 ± 6.5	St. 17	1.0	89.9	87.8	0.9
St. 18	Early tailbud	1.4	97.0 ± 1.2	132.5 ± 3.4	St. 19	1.2	103.0	120.3	1.0
St. 19	Mid-tailbud	1.9	113.6 ± 0.9	216.7 ± 15.7	St. 21	1.6	114.3	180.7	1.5
St. 20	Late tailbud I	2.3	118.6 ± 1.1	279.9 ± 18.9	St. 23	2.1	118.9	255.1	2.0
St. 21	Late tailbud II	4.3	127.0 ± 0.8	548.8 ± 7.3	St. 25	3.9	143.7	558.6	2.8
St. 22	Hatching larva	3.5	178.3 ± 3.0	641.7 ± 14.2	St. 26	4.2	159.3	661.6	3.0

Tail-to-trunk ratios and lengths of trunk and tail (each stage, $n = 3$) from seven stages of late neurula to hatching larva (stages 16–22) in *S. clava*. "Corresponding stage" corresponds to *C. robusta* at the same stage as *S. clava*. The data of *C. robusta* and *A. aspersa* are from the literature (Funakoshi et al. 2021; Hotta et al. 2007)

were photographed integrally using the tile function. Adobe Photoshop and ImageJ were used to pseudocolor the images. Embryos were fixed every 0.5–1 h from the fertilization of the egg to the hatching larva stage. Distinct representative embryos in each stage (Fig. 1) were chosen based on the *C. intestinalis* staging criteria from CLSM data (Hotta et al. 2007). Because of the dark color of *S. clava* embryos, the whole embryo could not be scanned directly, and only the fluorescence signal from appromaxiately half the thickness of the embryo could be received. Therefore, the 3D reconstructed images displayed in the Results section were all half embryos, and the ventral and dorsal images of the same period were from different individuals. Cortical actin filaments were stained using Alexa Fluor™ 488 Phalloidin (ThermoFisher, A12379).

Supplementary Information The online version contains supplementary material available at https://doi.org/10.1007/s42995-023-00200-2.

Acknowledgements This work was supported by the National Key Research and Development Program of China (2022YFC2601304; 2022YFC2601302), the Science & Technology Innovation Project of Laoshan Laboratory (LSKJ202203002), and the Taishan Scholar Program of Shandong Province, China (to BD). Database Construction was supported by the Research Institute of Marine Invertebrates (IKU2021-02), the Keio University Doctorate Student Grant-in-Aid Program from Ushioda Memorial Fund and JSPS KAKENHI Grant Number JP 22J22628, and Keio Gijuku Education with a Research-Adjusted Budget to TTS.

Author contributions BD conceived and guided the study. BL and WS collected the samples and performed the experiments. BL and WS prepared the figures and wrote the manuscript. TS constructed the website. QL assisted with defining the stages of embryogenesis. BD, QL, HY, and TS revised and edited the manuscript. All authors contributed to the article and approved the submitted version.

Data availability The authors declare that most datasets generated or analyzed during this study are included in this published article.

Declarations

Conflict of interest The authors declare that they have no conflicts of interest. Author Bo Dong is a member of the Editorial Board, but he was not involved in the journal's review of, or decision related to this manuscript.

Animal and human rights statement All of the procedures involved in the handling and treatment of ascidians in this study were approved by the Ocean University of China Institutional Animal Care and Use Committee (OUC-IACUC) prior to the initiation of the study (Approval number 2020–0082-0101, 8 September 2020). All experiments and relevant methods were carried out in accordance with the approved guidelines and regulations of OUC-IACUC.

References

Abbott DP, Johnson JV (1972) The ascidians *Styela barnharti*, *S. plicata*, *S. clava*, and *S. montereyensis* in Californian waters. Bull South Calif Acad Sci 71:95–105

Bhattachan P, Qiao R, Dong B (2020) Identification and population genetic comparison of three ascidian species based on mtDNA sequences. Ecol Evol 10:3758–3768

Brozovic M, Martin C, Dantec C, Dauga D, Mendez M, Simion P, Percher M, Laporte B, Scornavacca C, Di Gregorio A, Fujiwara S, Gineste M, Lowe EK, Piette J, Racioppi C, Ristoratore F, Sasakura Y, Takatori N, Brown TC, Delsuc F et al (2016) ANISEED 2015: a digital framework for the comparative developmental biology of ascidians. Nucl Acids Res 44:D808-818

Chiba S, Satou Y, Nishikata T, Satoh N (1998) Isolation and characterization of cDNA clones for epidermis-specific and muscle-specific genes in *Ciona savignyi* embryos. Zool Sci 15:239–246

Christiaen L, Wagner E, Shi W, Levine M (2009) Electroporation of transgenic DNAs in the sea squirt *Ciona*. Cold Spring Harb Protoc 4:pdb prot5345

Cinar ME (2016) The alien ascidian *Styela clava* now invading the Sea of Marmara (Tunicata: Ascidiacea). Zookeys 563:1–10

Cloney RA (1982) Ascidian larvae and the events of metamorphosis. Am Zool 22:817–826
Conklin EG (1905a) The mutation theory from the standpoint of cytology. Science 21:525–529
Conklin EG (1905b) Organization and cell lineage of the ascidian egg. Academy of Natural Sciences, Philadelphia
Corbo JC, Levine M, Zeller RW (1997) Characterization of a notochord-specific enhancer from the *Brachyury* promoter region of the ascidian, *Ciona intestinalis*. Development 124:589–602
Dardaillon J, Dauga D, Simion P, Faure E, Onuma TA, DeBiasse MB, Louis A, Nitta KR, Naville M, Besnardeau L, Reeves W, Wang K, Fagotto M, Gueroult-Bellone M, Fujiwara S, Dumollard R, Veeman M, Volff JN, Roest Crollius H, Douzery E et al (2020) ANISEED 2019: 4D exploration of genetic data for an extended range of tunicates. Nucl Acids Res 48:D668–D675
Davis MH, Davis ME (2010) The impact of the ascidian *Styela clava* Herdman on shellfish farming in the Bassin de Thau, France. J Appl Ichthyol 26:12–18
Dehal P, Satou Y, Campbell RK, Chapman J, Degnan B, De Tomaso A, Davidson B, Di Gregorio A, Gelpke M, Goodstein DM, Harafuji N, Hastings KE, Ho I, Hotta K, Huang W, Kawashima T, Lemaire P, Martinez D, Meinertzhagen IA, Necula S et al (2002) The draft genome of *Ciona intestinalis*: insights into chordate and vertebrate origins. Science 298:2157–2167
Delsuc F, Brinkmann H, Chourrout D, Philippe H (2006) Tunicates and not cephalochordates are the closest living relatives of vertebrates. Nature 439:965–968
Dumollard R, Minc N, Salez G, Aicha SB, Bekkouche F, Hebras C, Besnardeau L, McDougall A (2017) The invariant cleavage pattern displayed by ascidian embryos depends on spindle positioning along the cell's longest axis in the apical plane and relies on asynchronous cell divisions. eLife 6:e19290
Dupont L, Viard F, Dowell MJ, Wood C, Bishop JD (2009) Fine- and regional-scale genetic structure of the exotic ascidian *Styela clava* (Tunicata) in southwest England, 50 years after its introduction. Mol Ecol 18:442–453
Funakoshi HM, Shito TT, Oka K, Hotta K (2021) Developmental table and three-dimensional embryological image resource of the ascidian *Ascidiella aspersa*. Front Cell Dev Biol 9:789046
Goldstien SJ, Schiel DR, Gemmell NJ (2010) Regional connectivity and coastal expansion: differentiating pre-border and post-border vectors for the invasive tunicate *Styela clava*. Mol Ecol 19:874–885
Guignard L, Fiuza UM, Leggio B, Laussu J, Faure E, Michelin G, Biasuz K, Hufnagel L, Malandain G, Godin C, Lemaire P (2020) Contact area-dependent cell communication and the morphological invariance of ascidian embryogenesis. Science 369:6500
Hashimoto H, Robin FB, Sherrard KM, Munro EM (2015) Sequential contraction and exchange of apical junctions drives zippering and neural tube closure in a simple chordate. Dev Cell 32:241–255
Hibino T, Nishikata T, Nishida H (1998) Centrosome-attracting body: a novel structure closely related to unequal cleavages in the ascidian embryo. Dev Growth Differ 40:85–95
Hotta K, Dauga D, Manni L (2020) The ontology of the anatomy and development of the solitary ascidian *Ciona*: the swimming larva and its metamorphosis. Sci Rep 10:17916
Hotta K, Mitsuhara K, Takahashi H, Inaba K, Oka K, Gojobori T, Ikeo K (2007) A web-based interactive developmental table for the ascidian *Ciona intestinalis*, including 3D real-image embryo reconstructions: I. From fertilized egg to hatching larva. Dev Dyn 236:1790–1805
Jiang D, Smith WC (2007) Ascidian notochord morphogenesis. Dev Dyn 236:1748–1757
Kobayashi K, Satou Y (2018) Microinjection of exogenous nucleic acids into eggs: *Ciona* species. Adv Exp Med Biol 1029:5–13
Kogure YS, Muraoka H, Koizumi WC, Gelin-Alessi R, Godard B, Oka K, Heisenberg CP, Hotta K (2022) Admp regulates tail bending by controlling ventral epidermal cell polarity via phosphorylated myosin localization in *Ciona*. Development 149:dev200215
Kourakis MJ, Bostwick M, Zabriskie A, Smith WC (2021) Left/right asymmetry disruptions and mirror-image reversals to behavior and brain anatomy in *Ciona*. bioRxiv. https://doi.org/10.1101/2021.03.03.433807
Locke A, Hanson JM, Ellis KM, Thompson J, Rochette R (2007) Invasion of the southern Gulf of St. Lawrence by the clubbed tunicate (*Styela clava* Herdman): Potential mechanisms for invasions of Prince Edward Island estuaries. J Exp Mar Biol Ecol 342:69–77
Lu Q, Bhattachan P, Dong B (2019) Ascidian notochord elongation. Dev Biol 448:147–153
Lu Q, Gao Y, Fu Y, Peng H, Shi W, Li B, Lv Z, Feng XQ, Dong B (2020) *Ciona* embryonic tail bending is driven by asymmetrical notochord contractility and coordinated by epithelial proliferation. Development 147:24
Matsunobu S, Sasakura Y (2015) Time course for tail regression during metamorphosis of the ascidian *Ciona intestinalis*. Dev Biol 405:71–81
McDougall A, Chenevert J, Godard BG, Dumollard R (2019) Emergence of embryo shape during cleavage divisions. Results Probl Cell Differ 68:127–154
McDougall A, Chenevert J, Lee KW, Hebras C, Dumollard R (2011) Cell cycle in ascidian eggs and embryos. In: Kubiak JZ (ed) Cell cycle in development. Results and problems in cell differentiation. Springer, Berlin, Heidelberg, pp 153–169
Mizotani Y, Suzuki M, Hotta K, Watanabe H, Shiba K, Inaba K, Tashiro E, Oka K, Imoto M (2018) 14-3-3εa directs the pulsatile transport of basal factors toward the apical domain for lumen growth in tubulogenesis. Proc Natl Acad Sci USA 115:E8873–E8881
Negishi T, Takada T, Kawai N, Nishida H (2007) Localized PEM mRNA and protein are involved in cleavage-plane orientation and unequal cell divisions in ascidians. Curr Biol 17:1014–1025
Nicol D, Meinertzhagen IA (1988a) Development of the central nervous system of the larva of the ascidian, *Ciona intestinalis* L. I. The early lineages of the neural plate. Dev Biol 130:721–736
Nicol D, Meinertzhagen IA (1988b) Development of the central nervous system of the larva of the ascidian, *Ciona intestinalis* L. II. Neural plate morphogenesis and cell lineages during neurulation. Dev Biol 130:737–766
Nishida H (2005) Specification of embryonic axis and mosaic development in ascidians. Dev Dyn 233:1177–1193
Oonuma K, Tanaka M, Nishitsuji K, Kato Y, Shimai K, Kusakabe TG (2016) Revised lineage of larval photoreceptor cells in *Ciona* reveals archetypal collaboration between neural tube and neural crest in sensory organ formation. Dev Biol 420:178–185
Peng H, Qiao R, Dong B (2020) Polarity establishment and maintenance in ascidian notochord. Front Cell Dev Biol 8:597446
Sasaki H, Yoshida K, Hozumi A, Sasakura Y (2014) CRISPR/Cas9-mediated gene knockout in the ascidian *Ciona intestinalis*. Dev Growth Differ 56:499–510
Satoh N (1994) Developmental biology of ascidians. Cambridge University Press, New York
Satoh N (2013) A brief introduction to ascidians. In: Satoh N (ed) Developmental genomics of ascidians. Wiley-Blackwell, Hoboken, pp 1–7
Satou Y, Nakamura R, Yu D, Yoshida R, Hamada M, Fujie M, Hisata K, Takeda H, Satoh N (2019) A nearly complete genome of *Ciona intestinalis* type A (*C. robusta*) reveals the contribution of inversion to chromosomal evolution in the genus *Ciona*. Genome Biol Evol 11:3144–3157
Small KS, Brudno M, Hill MM, Sidow A (2007) Extreme genomic variation in a natural population. Proc Natl Acad Sci USA 104:5698–5703

Stolfi A, Gandhi S, Salek F, Christiaen L (2014) Tissue-specific genome editing in *Ciona* embryos by CRISPR/Cas9. Development 141:4115–4120

Swalla BJ (1993) Mechanisms of gastrulation and tail formation in ascidians. Microsc Res Tech 26:274–284

Tassy O, Dauga D, Daian F, Sobral D, Robin F, Khoueiry P, Salgado D, Fox V, Caillol D, Schiappa R, Laporte B, Rios A, Luxardi G, Kusakabe T, Joly JS, Darras S, Christiaen L, Contensin M, Auger H, Lamy C et al (2010) The ANISEED database: digital representation, formalization, and elucidation of a chordate developmental program. Genome Res 20:1459–1468

Villa LA, Patricolo E (2000) The follicle cells of *Styela plicata* (Ascidiacea, Tunicata): a sem study. Zoolog Sci 17:1115–1121

Wagner E, Stolfi A, Gi Choi Y, Levine M (2014) Islet is a key determinant of ascidian palp morphogenesis. Development 141:3084–3092

Wakai MK, Nakamura MJ, Sawai S, Hotta K, Oka K (2021) Two-round Ca2+ transient in papillae by mechanical stimulation induces metamorphosis in the ascidian *Ciona intestinalis* type A. Proc R Soc B 288:20203207

Wei J, Zhang J, Lu Q, Ren P, Guo X, Wang J, Li X, Chang Y, Duan S, Wang S, Yu H, Zhang X, Yang X, Gao H, Dong B (2020) Genomic basis of environmental adaptation in the leathery sea squirt (*Styela clava*). Mol Ecol Resour 20:1414–1431

Yamaji S, Hozumi A, Matsunobu S, Sasakura Y (2020) Orchestration of the distinct morphogenetic movements in different tissues drives tail regression during ascidian metamorphosis. Dev Biol 465:66–78

Zeller RW (2018) Electroporation in ascidians: history, theory and protocols. In: Sasakura Y (ed) Transgenic ascidians. Springer, Singapore, pp 37–48

Zhao L, Gao F, Gao S, Liang Y, Long H, Lv Z, Su Y, Ye N, Zhang L, Zhao C, Wang X, Song W, Zhang S, Dong B (2021) Biodiversity-based development and evolution: the emerging research systems in model and non-model organisms. Sci China Life Sci 64:1236–1280